International Journal of Thermal Sciences 48 (2009) 1914–1922

Contents lists available at ScienceDirect

International Journal of Thermal Sciences

journal homepage: www.elsevier.com/locate/ijts

Numerical and experimental study of three-dimensional fluid flow in the bipolar plate of a PEM electrolysis cell

Jianhu Nie [a,*], Yitung Chen [a], Steve Cohen [b], Blake D. Carter [b], Robert F. Boehm [a]

[a] Department of Mechanical Engineering, University of Nevada, 4505 Maryland Parkway, Las Vegas, NV 89154-4027, USA
[b] Distributed Energy Systems, Wallingford, CT 06492, USA

ARTICLE INFO

Article history:
Received 18 January 2008
Received in revised form
20 January 2009
Accepted 14 February 2009
Available online 19 March 2009

Keywords:
Bipolar plate
Proton exchange membrane (PEM)
Hydrogen production

ABSTRACT

The bipolar plate is one of the key components in proton exchange membrane (PEM) electrolysis cell stacks for hydrogen production. Bipolar plates of electrolysis cells must be properly designed to distribute reactant (water) evenly, and efficient PEM electrolysis cell stacks will require optimized bipolar plates. Numerical simulations and experimental measurements of three-dimensional water flow were performed for the purpose of examining pressure and velocity distributions in the bipolar plate of a PEM electrolysis cell. For the studied flow range, the computed pressure drops agree very favorably with the measurements. Results show that pressure decreases from the inlet tube to the exit tube along the diagonal direction. Both velocity and temperature distributions are very non-uniform in the channels. A minimum of the peak values of mainstream velocity component in the channels develops in the center of the test plate. The maximum of these peak values appears in the channel near the exit tube. For the studied flow levels, these lines along which the mainstream velocity component is a peak in the channel almost overlay with each other, except that minor difference can be noticed in the channel near the exit tube.

1. Introduction

The quality of human life depends to a large degree on the availability of energy resources, and hydrogen is expected to play an important role as an energy carrier of the future [1,2]. Hydrogen may be used as fuel in almost every application where fossil fuels are being used today, but without harmful emissions [3–5]. In particular, fuel cells are deemed as a key solution for the 21st century energy problems. However, hydrogen is not an energy source, and it does not occur in nature in its elemental or molecular form. Many methods have been developed for production of hydrogen using diverse resources including fossil fuels, biomass and renewable energy technologies [6–9]. Among these methods, electrolysis of water using proton exchange membrane (PEM) is considered a promising methodology for producing hydrogen in terms of its simplicity and specific production capacity.

Electrolysis is the process of using electricity to split water into hydrogen and oxygen. Water is split into oxygen, protons and electrons on one electrode (anode) by applying a DC voltage higher than the thermoneutral voltage. Protons pass through the polymer electrolyte membrane and on the cathode combine with electrons to form hydrogen. Passage of protons through the membrane is accompanied by water transport (electroosmotic drag). In electrolysis cells, the ions need to move quickly through the membrane to avoid the buildup of charge. In particular, the H^+ ions need to be transported from the working electrode where they are generated, through the membrane, to the counter-electrode where hydrogen is formed. The rate of hydrogen production is influenced by various parameters including temperature, velocity distributions, pressure distribution and current densities in the cell.

Although there are many studies on the theoretical analysis of fuel cells [10–14], not much has been reported on PEM electrolysis cells. In order to effectively design and use PEM electrolysis cells, analytical and/or numerical models for the device are necessary so that the system may be optimized. A series of experimental investigations on PEM water electrolysis applications have been reported by Millet et al. [15–17]. The design and assembly of the fuel cell stacks were tested and analyzed by Giddey et al. [18]. Badwal et al. [19] presented the results of PEM electrolysis for on-site, on-demand hydrogen production. Recent achievements and perspectives of PEM electrolysis systems were reviewed by Grigoriev et al. [20]. Onda et al. [21] provided a voltage–current relation wherein the cell voltage is described as the sum of Nernst voltage, resistive overpotential, and anode and cathode

* Corresponding author.
E-mail address: jianhu@nscee.edu (J. Nie).

1290-0729/$ – see front matter © 2009 Elsevier Masson SAS. All rights reserved.
doi:10.1016/j.ijthermalsci.2009.02.017

Nomenclature

C_p	specific heat
D_a	diameter of the inlet port
D_e	diameter of the exit port
h_a	height (or thickness) of the anodic channels
k	thermal conductivity
Q	flowrate
q_w	specific heat flux at wall
p	pressure
Re	Reynolds number
T	temperature
T_{in}	inlet temperature
x, y, z	coordinate directions
u	velocity component in x-coordinate direction
u_{in}	average velocity in the inlet pipe
v	velocity component in y-coordinate direction
w	velocity component in z-coordinate direction
w_m	average velocity based on the number of channels

Greek symbols

ρ	density
μ	dynamics viscosity

overpotentials. A simple model for electrochemical process in the water electrolysis cell was developed by Choi et al. [22]. Nie et al. [23,24] developed a photo-electrochemical model for PEM electrolysis cells with photo-anodes and examined effects of temperature and illumination intensity on power supply and hydrogen production rate. A dynamic model using Matlab–Simulink® for designing and analyzing sustainable energy systems was described by Gorgun [25]. A model was developed by Prince-Richard et al. [26] to determine the key technical and economic parameters influencing the competitive position of decentralized electrolytic hydrogen.

Similar to PEM fuel cell stacks, the bipolar plate is one of the key components in PEM electrolysis cell stacks, and it performs a number of essential functions in stack operation, such as reactant supply to the cell active area, current collection, and mechanical support to the MEA (membrane-electrode-assembly) part. Bipolar plates of electrolysis cell/stacks must be properly designed to distribute reactant (water) evenly across the catalyzed reaction surface area, in order to provide an efficient pathway to collect reaction products (hydrogen and oxygen), and to provide an electrical conduction path to the reaction sites. Thus, efficient PEM electrolysis cell stacks will require optimized bipolar plates. Improvements in the design of bipolar plates can help achieve the set goals of cost and performance for PEM electrolysis cells and stacks. Barreras et al. [27] demonstrated that the flow structure inside a bipolar plate can be visualized by applying laser-induced fluorescence in an optically accessible model. Flow in a PEM fuel cell bipolar plate with a diagonal structure was experimentally investigated by Lozano et al. [28]. It was shown that acetone vapor planar laser-induced fluorescence can be used to visualize the gas flow from the bipolar plate through the backing layer. Recently, Barreras et al. [29] studied flow distribution within three different bipolar plate geometries using laser-induced fluorescence trace tracking technique.

Although there are many PEM studies for fuel cell applications, very little research has been conducted for PEM electrolysis cells. Furthermore, most of the published numerical work is limited to two-dimensional cases [27,29]. However, flow in the actual systems is mostly three-dimensional. The present task is attempted to better understand the phenomena occurring within the bipolar plate PEM electrolysis cells so that the system may be optimized. Similar to fuel cells, optimization of the electrolysis cells is dependent of a set of complex physical and chemical processes occurring simultaneously. It has been demonstrated that these processes strongly depend on the fluid dynamics inside the cell [29]. The objective of present work is to perform three-dimensional simulations and experimental measurements of fluid flow in a bipolar plate of a simplified PEM electrolysis cell and to examine the flow dynamics inside it. Temperature distributions in the simplified bipolar plate will also be examined.

2. Problem statement and experimental descriptions

A schematic of the investigated bipolar plate PEM electrolysis cell is shown in Fig. 1. For clarity, only the fluid domain is displayed at the anode and cathode sides. The bipolar plate PEM electrolysis cell primarily consists of the water/oxygen channels (on the anode side), the water/hydrogen channels (on the cathode side), the gas diffusion layer at the anode side, the proton exchange membrane, and the gas diffusion layer at the cathode side. Obviously, a specific function of a bipolar plate is to produce a flow evenly distributed over the catalyzed electrodes. A low performance of the electrolysis cell conversion and a waste of the very expensive catalyst material could be expected if the flow distribution in the bipolar plate is non-uniform. For simplicity, because of the importance of fluid dynamics [27–29], emphasis is

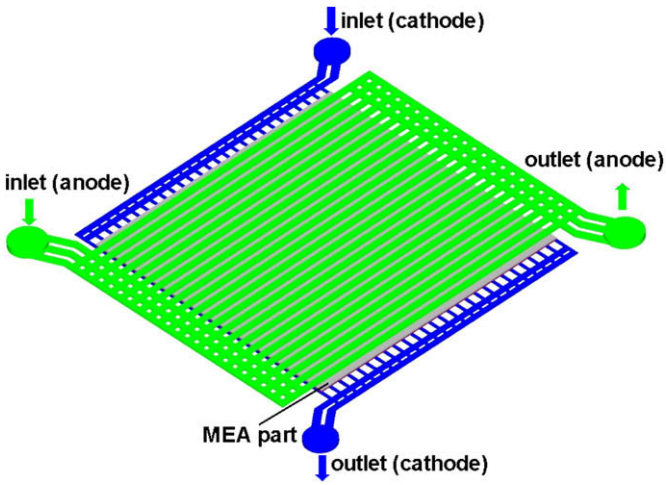

Fig. 1. Bipolar plates of PEM electrolysis cell for hydrogen production.

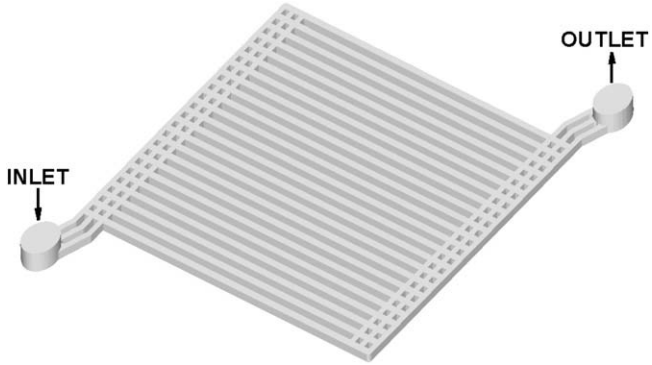

Fig. 2. Fluid domain within the anodic side of the bipolar plate.

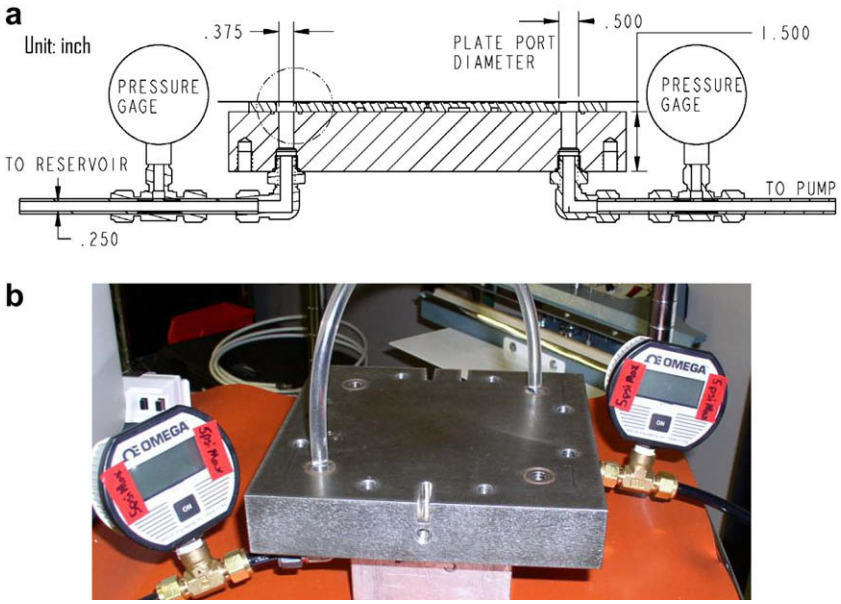

Fig. 3. Test part of the bipolar plate.

focused on the hydrodynamic analysis for the water flow inside the electrolysis cell. In the present manuscript, numerical and experimental investigations are restricted within only the anodic channels of the bipolar plate, as exhibited in Fig. 2. Water flows into the test plate through the inlet port and the manifold header. Many solid blocks are mounted in the inlet manifold header to enhance mechanical strength of the plate for operations under the high-pressure condition and to guide flow directions within the plate. Flow continues in the long channels next to the MEA part, where the electrochemical reaction occurs. Then, another manifold header with some solid blocks guides flow to exit from the outlet port. A physical test plate was made to perform verifications and validations. The test part of bipolar plate is shown in Fig. 3. The simplified test plate is machined from aluminum and it has 23 evenly distributed channels. Each channel has a cross-sectional area of 0.889 mm in height and 0.002 m in width. Diameters of the inlet (D_a) and the exit (D_e) are selected as the same ($D_a = D_e = 1.27$ cm).

A closed water loop was constructed to provide the desired flowrate. Two pressure gages are installed at the inlet and the exit ports to measure the pressure drop across the test plate. Water is supplied to the plate from a large water reservoir. It passes through a flowrate regulation system that maintains a desired and constant flowrate. The test part is connected to the pump and the water reservoir through plastic tubes with an inner diameter of 0.75 cm. The tubes are sufficiently long in order to ensure that flow inside the test plate is not influenced by the pump from the upstream or by the reservoir from the downstream. To ensure a steady state and stable flow conditions within the test plate, the mean flowrate was monitored. After ensuring that these flowrate measurements are repeatable, measurements were initiated for pressure drop across the test plate. The pressure drop was measured repeatedly to calculate the average pressure drop.

Table 1
Grid-independence test.

Grid	Elements	Nodes	w_1 (m/s)	p_1 (Pa)	w_2 (m/s)	p_2 (Pa)
1	4,238	9,040	−0.084	258	−0.169	104
2	9,220	15,420	−0.076	308	−0.169	131
3	106,161	161,130	−0.098	335	−0.185	142
4	171,222	226,135	−0.110	375	−0.213	163
5	355,552	438,486	−0.113	392	−0.224	173
6	648,860	767,740	−0.114	396	−0.228	176

3. Mathematical equations and numerical methods

The flow range in the present study is laminar, hydrodynamically stable and steady, where the Reynolds number based on the water flowrate and the inlet tube diameter (Re) is 50–600. The laminar three-dimensional Navier–Stokes and energy equations are solved numerically (using finite volume scheme) together with the continuity equation to simulate the flow, pressure and temperature fields.

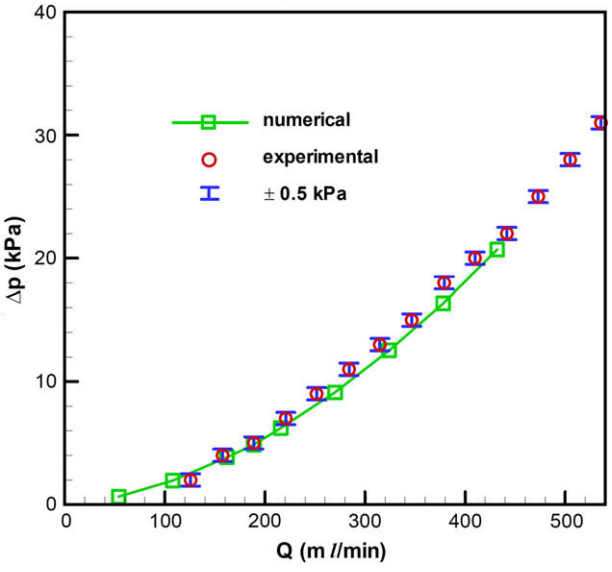

Fig. 4. Comparisons of the computed and the measured pressure drop.

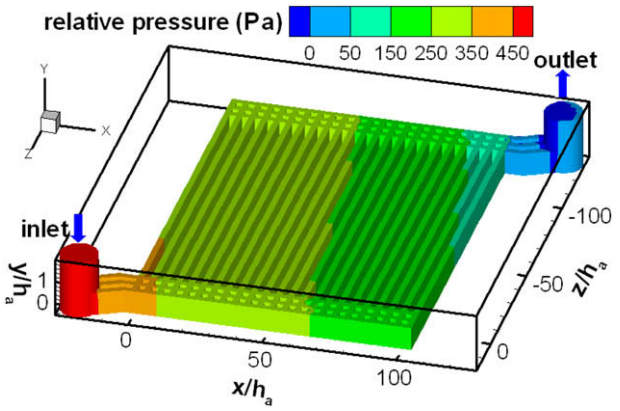

Fig. 5. Distribution of the pressure field ($h_a = 0.889$ mm).

Continuity equation:

$$\frac{\partial}{\partial x}(\rho u) + \frac{\partial}{\partial y}(\rho v) + \frac{\partial}{\partial z}(\rho w) = 0 \quad (1)$$

Momentum equations:

$$\frac{\partial}{\partial x}(\rho uu) + \frac{\partial}{\partial y}(\rho uv) + \frac{\partial}{\partial z}(\rho uw) = -\frac{\partial p}{\partial x} + \mu\left(\frac{\partial^2 u}{\partial x^2} + \frac{\partial^2 u}{\partial y^2} + \frac{\partial^2 u}{\partial z^2}\right) \quad (2)$$

$$\frac{\partial}{\partial x}(\rho uv) + \frac{\partial}{\partial y}(\rho vv) + \frac{\partial}{\partial z}(\rho vw) = -\frac{\partial p}{\partial y} + \mu\left(\frac{\partial^2 v}{\partial x^2} + \frac{\partial^2 v}{\partial y^2} + \frac{\partial^2 v}{\partial z^2}\right) \quad (3)$$

$$\frac{\partial}{\partial x}(\rho uw) + \frac{\partial}{\partial y}(\rho vw) + \frac{\partial}{\partial z}(\rho ww) = -\frac{\partial p}{\partial z} + \mu\left(\frac{\partial^2 w}{\partial x^2} + \frac{\partial^2 w}{\partial y^2} + \frac{\partial^2 w}{\partial z^2}\right) \quad (4)$$

Energy equation:

$$\frac{\partial}{\partial x}(\rho C_p uT) + \frac{\partial}{\partial y}(\rho C_p vT) + \frac{\partial}{\partial z}(\rho C_p wT) = k\left(\frac{\partial^2 T}{\partial x^2} + \frac{\partial^2 T}{\partial y^2} + \frac{\partial^2 T}{\partial z^2}\right) \quad (5)$$

where T is temperature, p is pressure, and u, v, and w are the velocity components in the x-, y-, and z-coordinate directions, respectively. The thermophysical properties are treated as constants and evaluated for water at 22 °C and 100 kPa (i.e., density (ρ) equals to 997.7 kg/m^3, dynamic viscosity (μ) is 9.61×10^{-4} kg/m s, specific heat (C_p) is 4181.2 J/kg °C and thermal conductivity (k) is 0.602 W/m °C). The inlet flow is assumed to be isothermal ($T_{in} = 22$ °C) with the desired flowrate, which is used to calculate

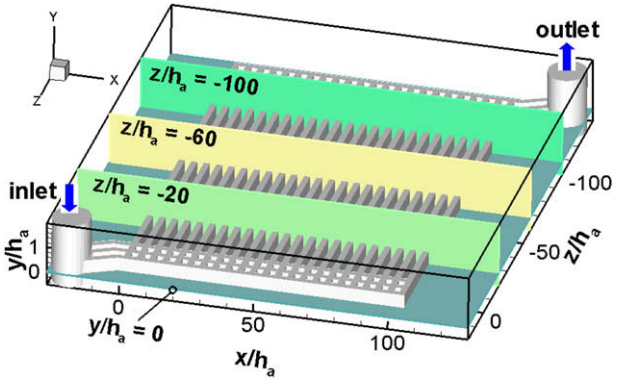

Fig. 6. Locations of the selected planes.

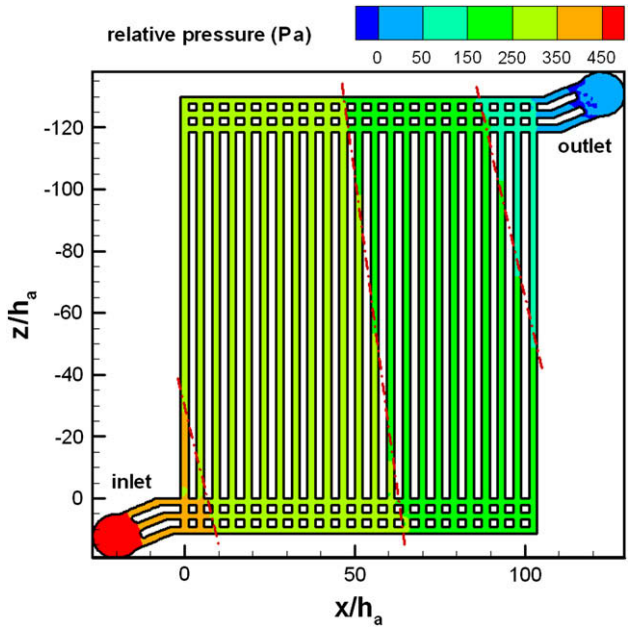

Fig. 7. Distribution of pressure field at the plane of $y/h_a = 0$.

the corresponding Reynolds number. At solid walls the boundary conditions are treated as no slip conditions (zero velocities). Pressure outlet flow condition is imposed at the exit section of the computational domain. For heat transfer modeling, all solid wall surfaces are assumed to be thermally adiabatic, except that the walls adjacent to the MEA (electrode-membrane-assembly) active area are specified with constant heat flux ($q_w = 2500$ W/m^2). This value of heat flux was obtained from experiments, which were performed in the separate work [30].

Numerical solution of the governing equations together with the applied boundary conditions was performed by utilizing the SIMPLE algorithm [31] for the pressure–velocity coupling in the iteration procedure. The QUICK scheme [32] is used to treat the convection transport and diffusion. Hexahedron volume elements

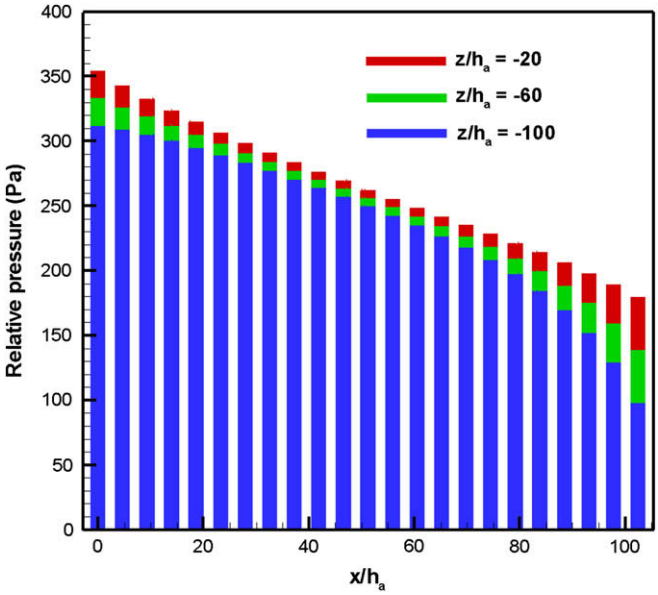

Fig. 8. Distributions of pressure along the spanwise x-direction ($y/h_a = 0$).

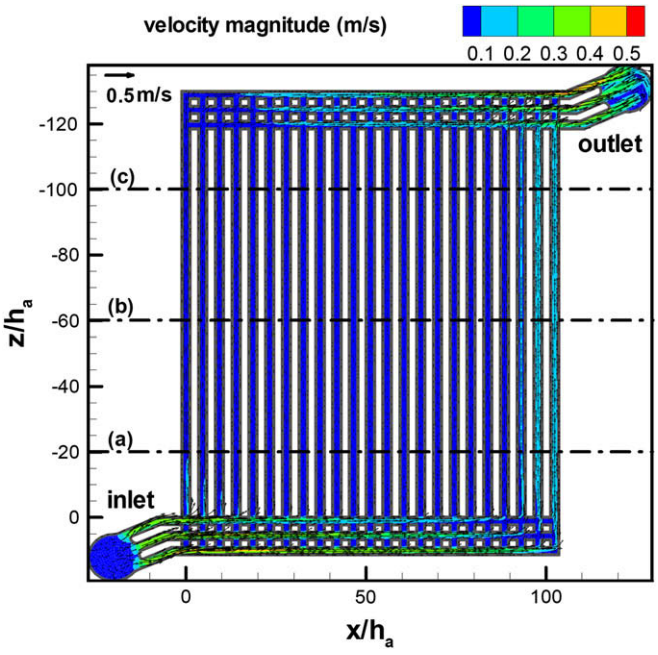

Fig. 9. Distribution of velocity field at the plane of $y/h_a = 0$.

are employed in the simulation, with finer mesh density near the solid walls and in the regions where the flow gradient is expected to be high. The CFD package, FLUENT, is used for solving the flow and pressure fields [33,34]. Grid-independence tests were performed using several grid densities and the w-velocity component and the pressure at two selected locations were used as the criteria for grid independence solution: Point 1 at $(0, 0, -0.05)$ and Point 2 at $(0.091, 0, -0.05)$. The results of grid-independence test are listed in Table 1. A grid with 355,552 elements and 438,486 nodes was finally selected for the numerical simulation. Using a larger grid with 648,860 elements and 767,740 nodes resulted in less than 2 percent difference in the predicted w-velocity component and the pressure at the selected locations. The residual sum for each of the conserved variables was monitored at the end of each iteration. The convergence criterion required that the maximum relative mass residual based on the inlet mass be smaller than 10^{-4}.

4. Results and discussions

Numerical simulations and experimental measurements were performed for three-dimensional water flow inside the anode side of the bipolar plate in a simplified PEM electrolysis cell. The computed pressure drop across the simplified bipolar plate was compared with the measured data, and they are displayed in Fig. 4. The agreement of the simulations with the experiments is very good, which justifies the present flow simulation model and provides confidence for the next simulations.

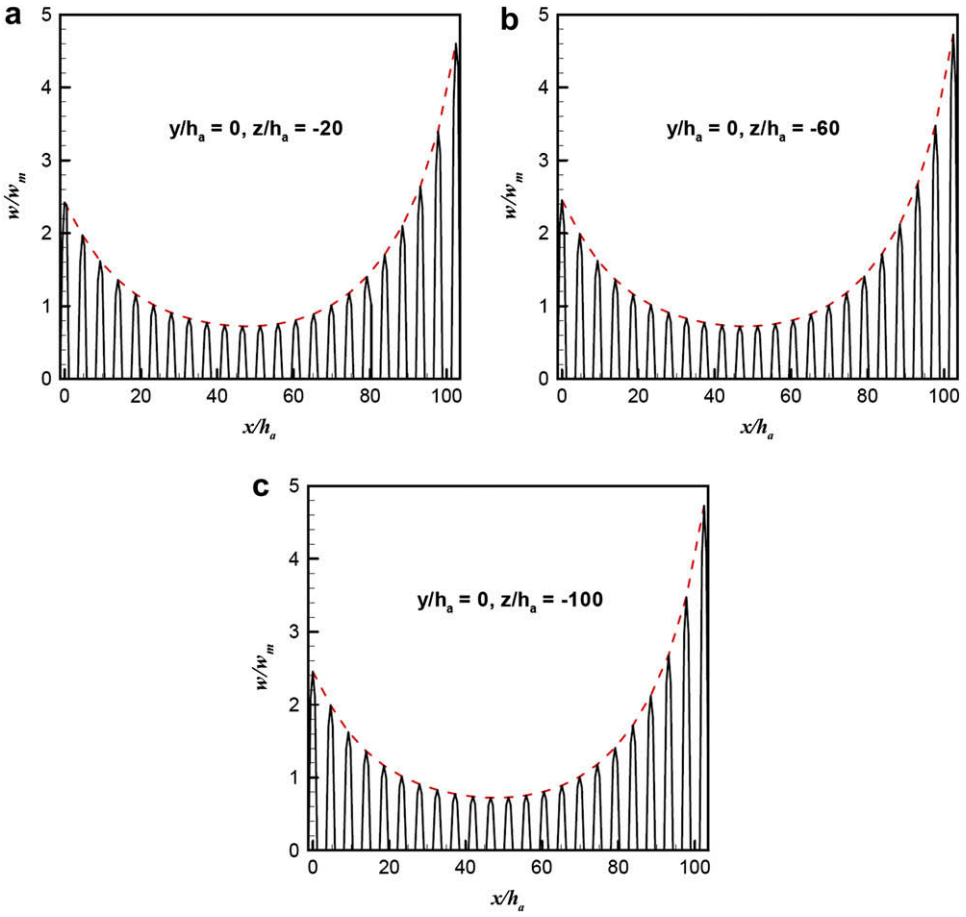

Fig. 10. Profiles of the w-velocity component along the x-direction.

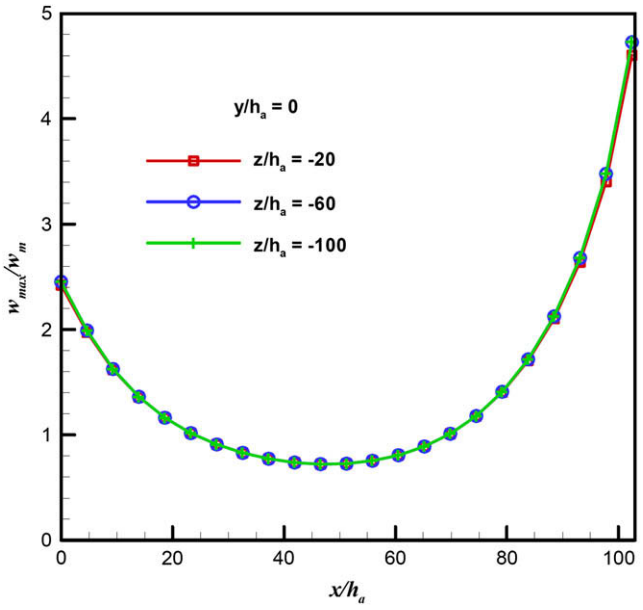

Fig. 11. Profiles of the peak *w*-velocity component in different channels.

Distribution of the pressure field for the flowrate of 60 ml/min is shown in Fig. 5. Numerical simulations were performed for the flowrates of 120 and 180 ml/min. The similar results are not included in the present manuscript because of space limitation. In Fig. 5, the dimensions are normalized based on the thickness (or height) of the bipolar plate channels ($h_a = 0.889$ mm). Because in the present work the pressure drop is of particular interest, only the relative pressure distribution is presented in this figure. It can be observed that the pressure drops diagonally from the inlet tube to the exit tube. The pressure drop is approximately 500 Pa for the flowrate of 60 ml/min. In addition, the pressure drop in the region near the inlet tube and the exit tube is relatively high because of the sudden change in geometry and flow direction.

For data visualization and presentation, several planes are selected and their locations are displayed in Fig. 6. It should be pointed out that the plane of $y/h_a = 0$ intersects the center height of the bipolar plate channels. Pressure distribution at the plane of $y/h_a = 0$ is given in Fig. 7. The dashed lines approximately represent the direction normal to the pressure drops. It also can be seen that the pressure drops diagonally from the inlet tube to the exit tube at this plane. Reverse flow develops in the region near the exit tube, where the relative pressure is negative. Distributions of pressure along the spanwise *x*-direction ($y/h_a = 0$), for $z/h_a = -20$, -60 and -100, are shown in Fig. 8. For the same *z*-location, pressure in the channels becomes lower from the inlet ($x/h_a \approx 0$) to the outlet ($x/h_a \approx 105$). In addition, the pressure drop along each channel can also be deduced from this figure using the pressure difference at different *z*-planes. Pressure drops are low along the channels in the middle of the test plate ($x/h_a \approx 50$), and they are high near the inlet and the outlet.

Distribution of the velocity field at the plane of $y/h_a = 0$ is presented in Fig. 9. Contours of the velocity magnitude are also included in this figure using different colors. The maximum velocity magnitudes develop in the regions near the inlet and the outlet,

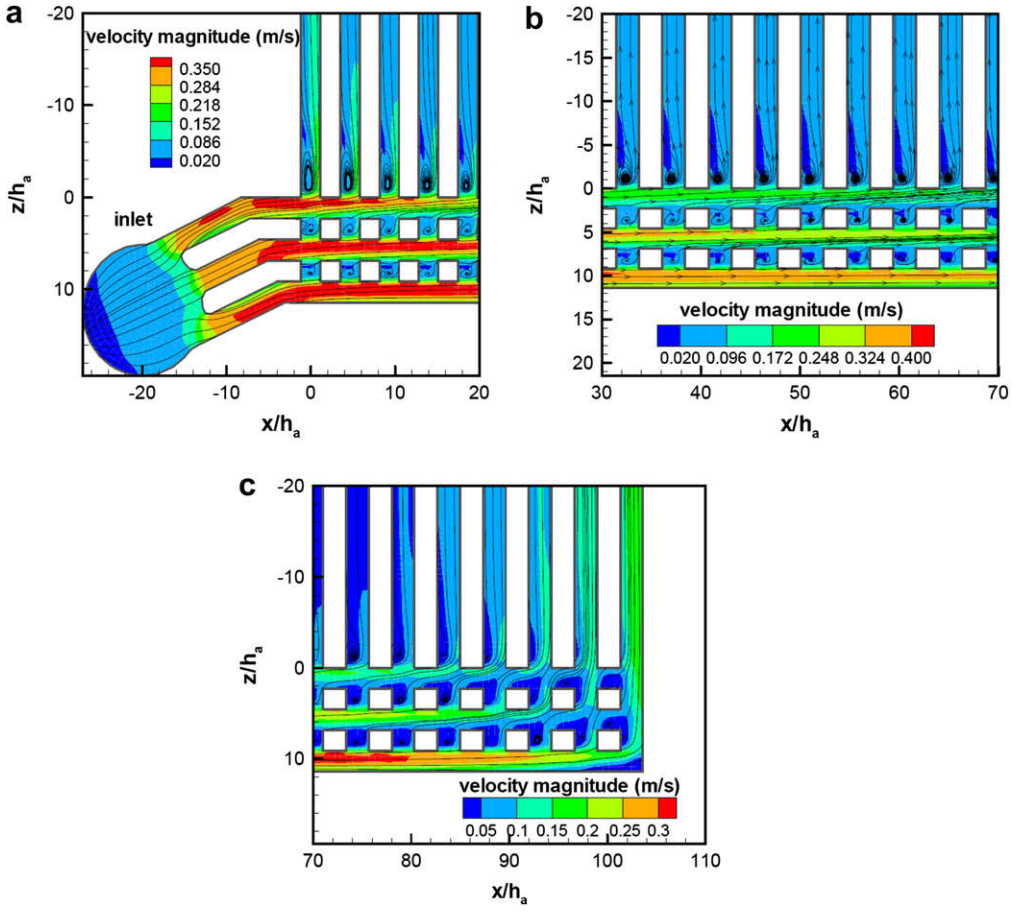

Fig. 12. Limiting streamlines inside the inlet manifold header section.

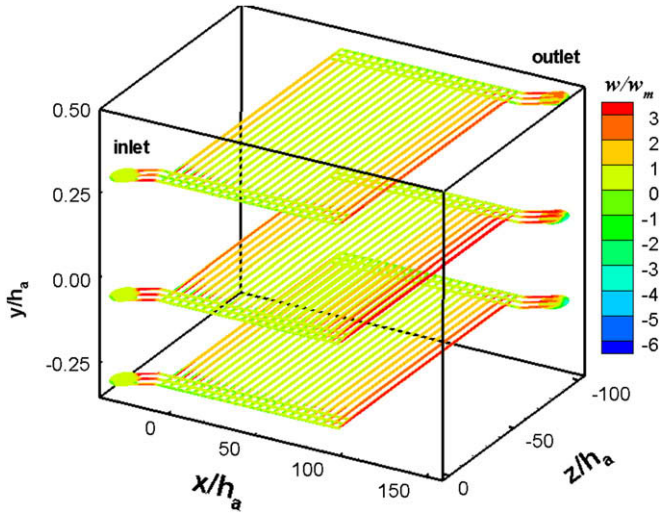

Fig. 13. Distribution of the *w*-velocity component at different *y*-planes.

where the pressure drops are relatively high (in Fig. 7). In contrast, velocity magnitude inside the channels is low, with higher flow velocity inside the channels close to the outlet. Reverse flow is observed in the exit tube and near the connection between the exit tube and the channels.

Fig. 10 shows profiles of the *w*-velocity component, which is the main velocity component along the channels, in the spanwise *x*-direction at several selected locations in order to examine the uniformity of velocity profile in the channels. Velocities in this figure are normalized based on the average velocity in each channel, which is obtained from the total flowrate divided by the channel's cross-sectional area and the number of channels. Therefore, ideally, the normalized velocity for this component shall be one if the velocity profile is perfectly evenly uniform in each channel. Positions of these locations can be referred to Figs. 6 and 9. The location of $y/h_a = 0$ is at the center height (or thickness) of the channels in the *y*-direction. The locations of $z/h_a = -20$ and -100 are near the inlet and the exit tubes, respectively, while the plane of $z/h_a = -60$ is approximately in the middle. It can be seen that, at all of these selected planes, the velocity distribution is very non-uniform across the test plate. The *w*-velocity component, which is the mainstream velocity component in the channels, is zero at the channel walls (the no-slip boundaries) and high at the center of the channels. The peak values in the channels are connected and denoted by the dashed line. A minimum of these peak values develops at about $x/h_a = 50$. The maximum of these peak values appears in the channel near the exit tube. The variations between the minimum and the maximum values can be as high as about 5.8 times. The velocity profiles at $y/h_a = 0$ and $z/h_a = -60$ do not differ much from those at $y/h_a = 0$ and $z/h_a = -100$, because the velocity profiles are almost fully-developed at these locations along the channels.

Profiles of the peak *w*-velocity component in different channels at the locations of $y/h_a = 0$ and $z/h_a = -20$, -60 and -100 are presented in Fig. 11. Although the velocity profiles in the channels may vary from each other, these peak values can still be used as a reference indication of the flowrate in each channel. These lines

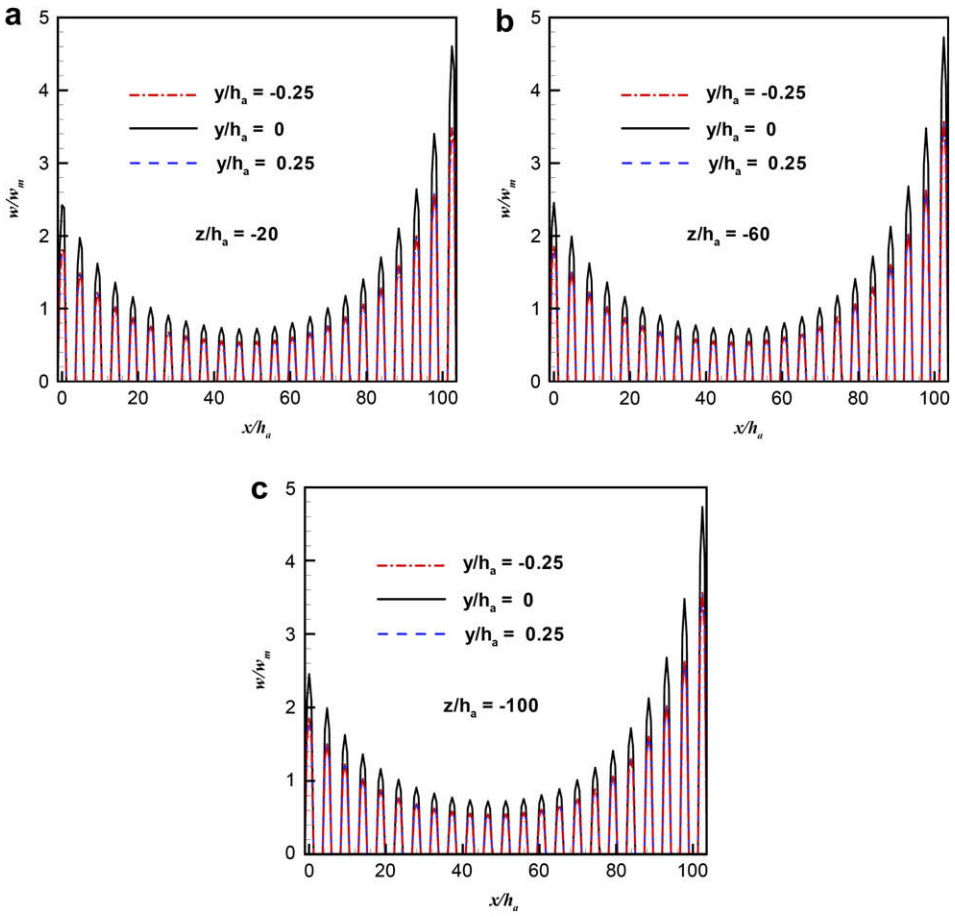

Fig. 14. Velocity profiles along the *x*-direction at different *y*-planes.

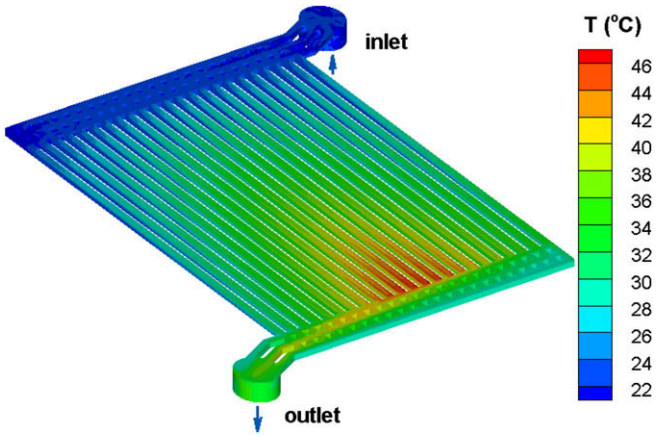

Fig. 15. Distribution of the temperature field.

almost overlay with each other, except that minor difference can be noticed in the channel near the exit tube. Therefore, it can be deduced that the total flowrate is far from being uniformly distributed in the layout and design of the bipolar plate channels. This provides an opportunity for improving design of the channels in the bipolar plate.

Limiting streamlines inside the inlet manifold header section are shown in Fig. 12. Flow recirculations can be observed at the beginning of the channels and between the solid blocks. The recirculating flow is not noticeable any more in the channels very close to the outlet, as exhibited in Fig. 12(*c*). Inside the three rows of flow channels in the manifold header and between the solid blocks, velocity magnitude is not evenly distributed: it is higher near the bottom boundary. From Fig. 12(*c*), it is found that flow in the bottom row is directly responsible for the high flow velocity inside the channels near the outlet.

Distributions of the *w*-velocity component at different *y*-planes ($y/h_a = -0.25$, 0 and 0.25) are shown in Fig. 13 in order to determine three-dimensionality of the flow field. It can be seen that velocity distributions at these three selected planes are very similar. At these planes, the *w*-velocity component is higher in the fluid channels close to the inlet and the exit. Relatively high *w*-velocity component is also observed to appear in the connection regions between the inlet and exit pipes and the header sections. Fig. 14 shows profiles of the *w*-velocity component along the *x*-direction at different *y*-planes. Velocity is high in the center of the channel ($y/h_a = 0$). The profiles at $y/h_a = -0.25$ and 0.25 for $z/h_a = -20$ almost overlay with each other, which shows that flow is becoming symmetric with respect to the center of channel ($y/h_a = 0$) and it is approximately fully developed in the channels at $z/h_a = -20$. This is also true for the velocity profiles at other *z*-planes ($z/h_a = -60$ and -100). Effect of flow entry is not very significant for the flow development in the channels at the selected locations ($z/h_a = -20$, -60 and -100).

Temperature distribution viewed from the membrane-electrode-assembly (MEA) part is given in Fig. 15. In general, temperature increases from the inlet section to the exit section as a result of the heating from the heat flux at the MEA part. However, the maximum temperature does not appear in the exit. It develops inside the fluid channels and close to the header section at the side of exit port. This is because fluid adjacent to the MEA part is heated directly and temperature of this fluid layer increases first. As fluid enters the header section, it is further mixed with the cooler fluid in other part of the fluid channels. Therefore, the average temperature of fluid becomes lower inside the header section near the exit ports. This leads to the development of maximum temperature of fluid upstream and close to the exit header section. It also can be seen that temperature distribution is not uniform. It is relatively high in the center of plate and near the exit header section.

5. Conclusions

Numerical simulations of three-dimensional water flow together with experimental measurements were performed for the purpose of examining pressure and velocity distributions in the bipolar plate of a PEM electrolysis cell. The numerical results show that the pressure drops diagonally from the inlet tube to the exit tube. The pressure drop in the region near inlet tube and the exit tube is relatively high. Reverse flow is observed in the exit tube and near the connection between the exit tube and the channels. Both the velocity and the temperature distributions in the channels are very non-uniform over the test plate. A minimum of the peak values of mainstream velocity component in the channels develops in the middle of the plate. The maximum of these peak values appears in the channel near the exit tube. The lines along which the mainstream velocity component is a peak in the channel almost overlay with each other, except that minor difference can be noticed in the channel near the exit tube. This provides opportunity for overall control and optimum design of the channels in the bipolar plate.

Acknowledgements

This work was supported by US Department of Energy under award DE-FG36-03GO13063.

References

[1] K. Adamson, Hydrogen from renewable resources – the hundred year commitment, Energy Policy 32 (2004) 1231–1242.
[2] J.M. Ogden, Hydrogen: the fuel of the future? Physics Today 55 (2002) 69–75.
[3] D. Morgan, F. Sissine, Hydrogen: Technology and Policy, Congressional Research Service, Report for Congress, The Committee for the National Institute for the Environment, 1995.
[4] T.N. Veziroglu, Dawn of the hydrogen age, International Journal of Hydrogen Energy 23 (1998) 1077–1078.
[5] V.A. Goltsov, T.N. Veziroglu, From hydrogen economy to hydrogen civilization, International Journal of Hydrogen Energy 26 (2001) 909–915.
[6] J.A. Turner, A realizable renewable energy future, Science 285 (1999) 687–689.
[7] M. Momirlan, T.N. Veziroglu, Current status of hydrogen energy, Renewable and Sustainable Energy Reviews 6 (2002) 141–179.
[8] S. Dunn, Hydrogen future: toward a sustainable energy system, International Journal of Hydrogen Energy 27 (2002) 235–264.
[9] F. Barbir, PEM electrolysis for production of hydrogen from renewable energy sources, Solar Energy 78 (2005) 661–669.
[10] J. Larmineand, A. Dicks, Fuel Cell Systems Explained, John Wiley & Sons, New York, NY, 2000.
[11] D. Cheddie, N. Munroe, Review and comparison of approaches to proton exchange membrane fuel cell modeling, Journal of Power Sources 147 (2005) 72–84.
[12] K. Scott, W. Taama, J. Cruickshank, Performance and modelling of a direct methanol solid polymer electrolyte fuel cell, Journal of Power Sources 65 (1997) 159–171.
[13] T.V. Nguyen, R.E. White, A water and heat management model for proton-exchange-membrane fuel-cells, Journal of the Electrochemical Society 140 (1993) 2178–2186.
[14] W.Q. Tao, C.H. Min, X.L. Liu, Y.L. He, B.H. Yin, W. Jiang, Parameter sensitivity examination and discussion of PEM fuel cell simulation model validation – part I. Current status of modeling research and model development, Journal of Power Sources 160 (2006) 359–373.
[15] P. Millet, T. Alleau, R. Durand, Characterisation of membrane-electrode assemblies for solid polymer electrolyte water electrolysis, Journal of Applied Electrochemistry 23 (1993) 322–331.
[16] P. Millet, Water electrolysis using EME technology – electric-potential distribution inside a Nafion membrane during electrolysis, Electrochimica Acta 39 (1994) 2501–2506.
[17] P. Millet, F. Andolfatto, R. Durand, Design and performance of solid polymer electrolyte water electrolyzer, International Journal of Hydrogen Energy 21 (1996) 87–93.
[18] S. Giddey, F.T. Ciacchi, S.P.S. Badwal, Design, assembly and operation of polymer electrolyte membrane fuel cell stacks to 1 kW_e capacity, Journal of Power Sources 125 (2004) 155–165.

[19] S.P.S. Badwal, S. Giddey, F.T. Ciacchi, Hydrogen and oxygen generation with polymer electrolyte membrane (PEM)-based electrolytic technology, Inoics 12 (2006) 7–14.
[20] S.A. Grigoriev, V.I. Porembsky, V.N. Fateev, Pure hydrogen production by PEM electrolysis for hydrogen energy, International Journal of Hydrogen Energy 31 (2006) 171–175.
[21] K. Onda, T. Murakami, T. Hokosaka, M. Kobayashi, R. Notu, K. Ito, Performance analysis of polymer-electrolyte water electrolysis cell at a small-unit test cell and performance prediction of large stacked cell, Journal of the Electrochemical Society 149 (2002) A1069–A1078.
[22] P. Choi, D.G. Bessarabov, R. Datta, A simple model for solid polymer electrolyte (SPE) water electrolysis, Solid State Ionics 175 (2004) 535–539.
[23] J.H. Nie, Y.T. Chen, R.F. Boehm, S.P. Katukota, A photoelectrochemical model of proton exchange water electrolysis for hydrogen production, ASME Journal of Heat Transfer 130 (4) (2008) 042409 (6 pages).
[24] J.H. Nie, S.P. Katukota, Y.T. Chen, R.F. Boehm, H.T. Hsieh, A photo-electrochemical model of solid polymer water electrolysis for hydrogen production from sunlight, in: Proceedings of 1st Energy Nanotechnology International Conference, ENIC2006-19039, Massachusetts Institute of Technology (MIT), Cambridge, MA, USA, 2006.
[25] H. Gorgun, Dynamic modelling of a proton exchange membrane (PEM) electrolyzer, International Journal of Hydrogen Energy 31 (2006) 29–38.
[26] S. Prince-Richard, M. Whale, N. Djilali, A techno-economic analysis of decentralized electrolytic hydrogen production for fuel cell vehicles, International Journal of Hydrogen Energy 30 (2005) 1159–1179.
[27] F. Barreras, A. Lozano, L. Valiño, C. Marín, A. Pascau, Flow distribution in a bipolar plate of a proton exchange membrane fuel cell: experiments and numerical simulation studies, Journal of Power Sources 144 (2005) 54–66.
[28] A. Lozano, F. Barreras, L. Valiño, C. Marín, Imaging of gas flow through a porous medium from a fuel cell bipolar plate by laser-induced fluorescence, Experiments in Fluids 42 (2006) 301–310.
[29] F. Barreras, A. Lozano, L. Valiño, R. Mustata, C. Marín, Fluid dynamics performance of different bipolar plates: part I. Velocity and pressure fields, Journal of Power Sources 175 (2008) 841–850.
[30] J.H. Nie, J.F. Wu, S. Cohen, B. Carter, Y.T. Chen, Numerical simulations of coupled flow and heat transfer distributions in a bipolar plate of the PEM electrolysis cell, in: Proceedings of ASME Heat Transfer, Fluids, Energy, Solar & Nano Conferences, FEDSM2008-55188, Jacksonville, FL, August 10–14, 2008.
[31] S.V. Patankar, Numerical Heat Transfer and Fluid Flow, Hemisphere, New York, NY, 1980.
[32] B.P. Leonard, Elliptic systems: finite difference method IV, in: W.J. Minkowycz, et al. (Eds.), Handbook of Numerical Heat Transfer, Wiley, New York, 1988, pp. 347–378.
[33] J.H. Nie, Y.T. Chen, S. Cohen, B. Carter, R.F. Boehm, Non-uniform velocity distributions in bipolar plate PEM electrolysis cell, in: Proceedings of 5th Joint ASME/JSME Fluids Engineering Conference, FEDSM2007-37299, San Diego, CA, July 31–August 2, 2007.
[34] J.H. Nie, Y.T. Chen, R.F. Boehm, Numerical modeling of two-phase flow in a bipolar plate of a PEM electrolysis cell, in: Proceedings of ASME International Mechanical Engineering Congress and Exposition, IMECE2008-68913, Boston, MA, November 2–6, 2008.